

A portable diagnosis model for Keratoconus using a smartphone

Yifan Li^a, Myeongjun Kim^b, Yanjing, Jin^b Peter Ho^c, Jo Woon Chong^d

^a Department of Electrical and Computer Engineering, Texas Tech University, Lubbock, USA,

^b Department of Electrical and Computer Engineering, Sungkyunkwan University, Suwon, South Korea,

^c Lubbock Eye Clinic, Lubbock, Texas 79410, USA

^d School of Electronic and Electrical Engineering, Sungkyunkwan University, Suwon, South Korea,

jwchong@skku.edu

Abstract

Keratoconus (KC) is a progressive corneal disorder characterized by localized thinning and protrusion, leading to visual distortion. While Placido disc-based topography remains a standard in clinical diagnostics, its dependence on specialized equipment limits accessibility. In this paper, we propose a portable, smartphone-based diagnostic framework that captures corneal reflections of a Placido disc displayed on a phone screen and applies a two-stage detection pipeline, then validate on 3D-printed emulated eyeball models that simulate normal, moderate, and severe KC stages based on anterior chamber depth (ACD). The first step of the two-stage detection pipeline is classifying different stages of KC with features including height and width of extracted reflections using weighted support vector machine (WSVM). It achieves a maximum accuracy of 92.93%, and maintains over 90% accuracy across multiple smartphone models, including the Galaxy Z Flip 3, iPhone 15 Pro, and iPhone 16 Pro. For the second step, we visualize the KC-affected protrusion regions on the corneas with color maps based on inter-disc distance, that provides an intuitive representation of disease severity and localization. Moreover, we validate the ability of the extracted features to differentiate between KC stages with ANOVA and Omega Squared, with significant p-values (e.g., $p < 10^{-6}$) and large effect sizes (ω^2 up to 0.8398) among classes.

Keywords

Keratoconus, Smartphone diagnosis, Placido disc, WSVM (Weighted Support Vector Machine), corneal topography, image processing, 3D-printed model

1. Introduction

Keratoconus (KC) is a corneal disorder causing blurry and distorted vision from thinning and steepening of the cornea, as shown in Figure 1a (Rabinowitz, 1993, 1998). The potential risk factors of KC are corneal thinning and subsequent steepening associated with Down syndrome, atopy, eczema, excessive eye rubbing, and genetic disorders (Gordon-Shaag et al., 2015; Karolak & Gajecka, 2017). Moreover, environmental factors, such as long-lasting ultraviolet light exposure and hot climate in some Asian countries such as India, may result in an increase in the number of KC subjects compared to other parts of the world (Assiri et al., 2005; Nielsen et al., 2007).

The most prevalent method for diagnosing KC is monitoring clinical signs such as Vogt striae, Rizzuti signs, Munson signs, Fleischer rings, and the retinoscopy scissoring reflex by using slit-lamp examination (Jonas et al., 2009). These methods can quickly diagnose moderate to advanced cases of KC. However, the early detection of KC helps to prevent vision loss or the need for corneal transplantation, i.e., timely intervention with corneal cross-linking (CXL) can be performed before the cornea has thinned excessively, and early detection can help avoid complications associated with advanced keratoconus (Belin et al., 2022). To detect mild stages of KC with higher accuracy, a series of corneal topography technologies, for instance, Placido disc, photo-keratoscopy, keratometry, and computer-assisted video-keratography (Bevara & Vaddavalli, 2023; De Sanctis et al., 2007; Gordon-Shaag et al., 2012) have been widely used. Scheimpflug imaging, optical coherence tomography, and slit-scan tomography have also been used for KC early detection (Buzzonetti et al., 2020). The diagnostic methodologies discussed thus far necessitate using advanced clinical devices for data collection. These instruments, however, have limitations in that they could be inconvenient and may require a skilled technician for operation and maintenance. Furthermore, for an accurate and reliable Keratoconus (KC) diagnosis, ophthalmologists and optometrists should concurrently consider various other clinical indicators of the disease (Agrawal, 2011).

Utilizing advancements in machine learning, image processing technologies, and smartphones' ubiquity, we can now develop accurate and easy-to-use imaging and diagnosis methods. For example, the brilliant KC consists of a 3D-printed Placido disc attachment, an LED light strip, and an intelligent app capturing the reflection of Placido rings

(Askarian et al., 2018). It utilizes an image processing pipeline to analyze the corneal image and applies the smartphone's camera parameters, Placido rings' 3D location, and pixel location of reflected rings for the KC diagnosis (Gairola et al., 2021). Another novel feature of our approach is capturing side photos of the eyes, processing these images to analyze corneal curvature at various angles, and identifying keratoconus based on the differences observed. This method is adaptable to multiple smartphone types with high detection accuracies for severe to moderate keratoconus (Askarian et al., 2018).

Placido-based corneal topography systems project the concentric Placido rings onto the cornea and analyze the reflection to assess the anterior corneal surface. (Gao et al., 2020). KC is characterized by localized corneal thinning and protrusion, leading to a distinctive distortion of the reflected rings and changes in the inter-ring distance, which are regarded as KC hallmarks and a primary diagnostic indicator. While other corneal conditions can influence the Placido disc reflection patterns, their effects on inter-ring distances are generally less obvious or perform differently. For example, corneal scars and degenerations cause surface irregularities, resulting in localized distortions of the reflected rings. However, these distortions are usually limited to the areas of scarring and do not present the progressive inter-ring distance changes characteristic of KC (Seitz et al., 1997). An unstable or disrupted tear film can affect the quality of Placido disc reflections, leading to artifacts or irregular patterns, but these changes are usually diffuse and transient (Fu et al., 2020). In this study, our method is designed to detect the changes from KC.

In this paper, we propose a portable and easy-to-use methodology for diagnosing Keratoconus (KC). Our method leverages smartphones' versatility for detecting KC and image processing and machine learning techniques for pinpointing the corneal region affected by the disease. As illustrated in Figure 1b, our procedure does not require a 3D-printed attachment; instead, we display a Placido disc on the smartphone's screen, directed towards the patient's eye, and capture images of the discs reflected from the cornea. This novel approach aids in not only identifying KC but also visualizing the affected area of the cornea. Fig 1c shows a broader view of our method where the Placido disc is displayed on a smartphone's screen and smartphone's camera then captures images of the reflected discs from a left eye. We proposed enhanced the Placido disc's design, as shown in Fig 1d-i, where the center ring has been transformed into a solid circle to facilitate graphic visualization on the cornea. Fig 1d-ii exhibits' images obtained from a normal cornea, a moderate KC effected cornea and a severe KC effected cornea in our experiments. We applied an image processing pipeline to extract meaningful diagnostic features from the captured images, including specular reflection

removal, disc extraction, and geometric feature measurement (width and height). A two-stage framework was employed for KC severity classification and protrusion region visualization after feature extraction. In the first stage, we applied multiclass Weighted Support Vector Machine (WSVM) to classify the corneas into normal, moderate KC, and severe KC categories, achieving a maximum accuracy of 92.93% and maintaining over 90% accuracy across multiple smartphone models. In the second stage, we generated color-coded distance maps based on inter-disc measurements to visualize KC protrusion's precise location and severity. Statistical analyses, including ANOVA and Omega Squared (ω^2 up to 0.8398), confirmed the effectiveness of the extracted features in distinguishing disease stages.

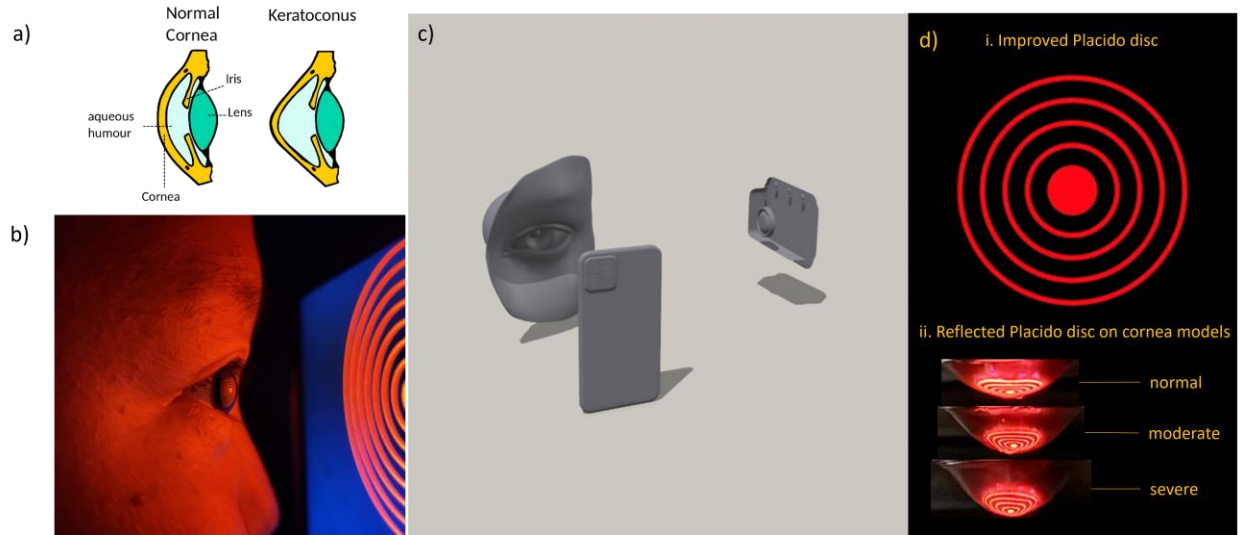


Figure 1. Overview of portable Keratoconus diagnosis. **a)** Demonstration of the non-KC eye and KC eye with the cone-shaped cornea. **b)** Concept of the proposed approach. **c)** Overview of smartphone-based Placido disc reflection capture system. **d)** i. Improved Placido disc and ii. Reflections on the Placido disc on cornea models over normal, moderate-KC , and severe-KC stage.

2. Method

2.1. Design of image capturing model

Corneal curvature describes how steep (or flat) the surface of the cornea is at a given point. It is typically measured in diopters (D) using instruments such as keratometry or Placido-based topographers (Cavas-Martínez et al.; Shirayama et al., 2010). For instance, the Keratoconus eyes can be divided into moderate (47.0 to 52.0 D), and severe (52.0 D or

higher) according to mean curvature (Emre et al., 2007; Hashemi et al., 2020). In topographic systems, increased curvature is associated with steeper surfaces, resulting in compressed or distorted projected rings and reflection patterns. In keratoconus corneas, these distortions are localized, especially in inferior or central zones, making curvature a critical geometric and diagnostic feature. In order to create a model fitting the human cornea, we used anterior the chamber depth (ACD). As shown in Figure 2, ACD, defined as the distance from the corneal endothelium to the anterior lens surface, has been proven to increase with KC severity due to forward displacement of the corneal apex (Emre et al., 2007), which allows us to simulate varying KC stages with more anatomical fidelity physically.

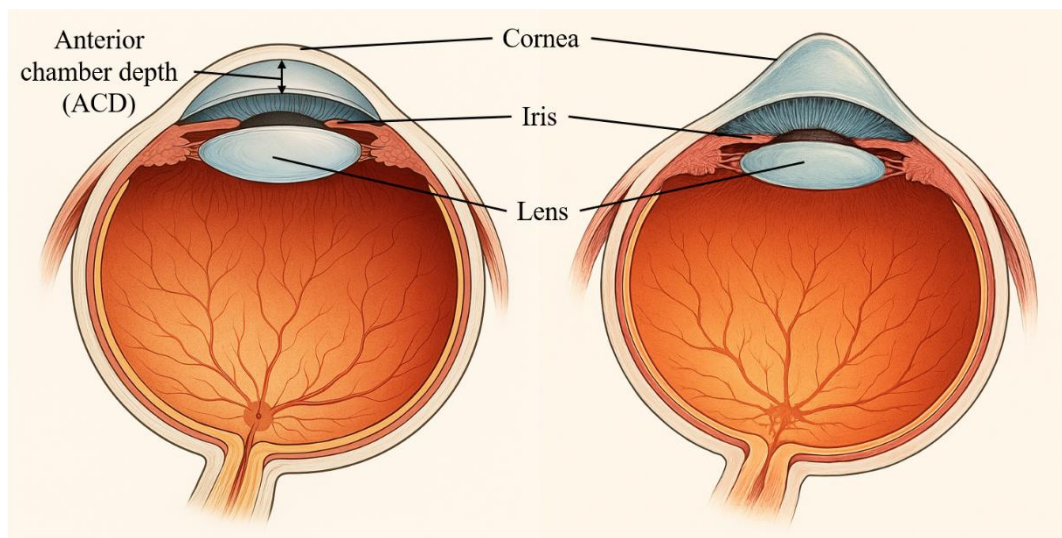


Figure 2. Difference between normal and Keratoconus cornea, Anterior chamber depth (ACD) increases due to Keratoconus.

In this study, we designed and printed emulated eyeballs for each type of eye: 1) normal, 2) moderate KC, and 3) severe KC, based on ACD, using a 3D printer as shown in Table 1. Considering the variety of real eyeballs, we designed three versions (smaller, medium, and larger) for each stage of KC (Hashemi et al., 2020; Kovács et al., 2010).

Anterior chamber depth (mm)			
	Small	Medium	Large
Normal	2.54	2.7025	2.865

Moderate KC	3.0275	3.19	3.3525
Severe KC	3.515	3.6775	3.84

Table 1. Anterior chamber depth measurements for emulated eyeball models across different sizes (small, medium, and large) and stages (normal, moderate KC, and severe KC) of Keratoconus.

In corneal topography, particularly with Placido disc systems, the cornea's anterior surface acts as a convex mirror, reflecting light to the imaging system. This method primarily captures the shape and curvature of the cornea by analyzing these reflections (Mejía-Barbosa & Malacara-Hernández, 2001; Wang, 2024). In this case, light reflecting off the anterior corneal surface is the primary measurement. To quantify when internal refraction can be ignored, we considered the geometry of the system, according to Snell's Law as shown in Eq. 1 (Næser et al., 2016):

$$n_1 \sin(\theta_1) = n_2 \sin(\theta_2) \quad (1)$$

where n_1 and n_2 are refractive indexes of the first and second medium (air: $n_1 \approx 1.000$, cornea $n_2 \approx 1.376$), θ_1 and θ_2 represent the angle of incidence and refraction. In the case of corneal topography, the light rays strike the cornea nearly perpendicularly. Since the sine of the angle is approximately equal to the angle itself when measured in radians ($\sin(\theta) \approx \theta$) for small angles, we could obtain the difference between θ_1 and θ_2 is minimal by applying this approximation in Eq. 2:

$$n_1 \theta_1 \approx n_2 \theta_2 \quad (2)$$

In addition, optical path length (OPL) within the cornea is the actual distance light travels inside the cornea (Farjo et al., 2009), which is given in Eq. 3:

$$OPL = n_2 \times d \quad (3)$$

where d represents physical thickness of the cornea (0.5 mm centrally), n_2 is the refractive index of the cornea which gives an approximate OPL value of 0.688mm.

By applying Snell's Law and considering the small-angle approximation along with the optical path length within the cornea relative to the observation distance, we can justify that the effects of light refraction within the cornea are

negligible in setups where the light source and camera are positioned significantly farther from the cornea (150 mm) than the cornea's thickness.

Since the standard 3D printing materials used for the eyeball models lack reflective properties, we applied a reflective coating to the corneal region of each eyeball model. This simulates the reflective behavior of the anterior corneal surface, ensuring that the corneal region has the necessary reflectivity to capture Placido disc patterns.

In our experimental setup, we modified the camera positioning compared to traditional diagnostic methods, as illustrated in Figure 3a. Instead of aligning the camera and light source along the same optical axis, we positioned the camera at a 90-degree angle relative to the light source to better capture the reflected Placido disc patterns. While a foldable smartphone could theoretically integrate both functions displaying the Placido disc and capturing its reflection on separate screens - our implementation utilized two separate smartphones: one serving as the light source and the other functioning as the imaging device. This configuration ensures flexibility, enabling the method to be implemented using any standard smartphone setup rather than relying on foldable devices. In Figure 3a, the cornea curve C faces the light source plane P_G , we capture the images at the plane P_C which is perpendicular to P_G steps away from the conventional same-axis method, 3b, where the camera locates on P_G and the face's center of C . The experimental setting of P_C and P_G is shown in Figure 3c, the green line represents the camera P_C and the blue line represents the Placido disc displaying screen P_G . The various notations in Figures 3a and 3b have specific implications, which will be clarified in the following discussion. A and B correspond to any two different circles (ignore the width of the circles), A' and B' are the points of incidence from the incident rays AA' and BB' . Correspondingly, $A'A''$ and $B'B''$ are the reflected rays from cornea model to the plane of camera, A'' and B'' are the images of corresponding circle we obtain from the camera which means the length of the line $A''B''$ (d'') is the distance between the two corresponding circles observed on camera. Based on the schematic diagram of image capturing, we hypothesize the distance (d'') that Placido discs are related to the severity of Keratoconus, as shown in Eq. 4.

$$d'' = (h_{B'} - h_{A'}) + l \left(\tan 2\alpha - \frac{1}{\tan 2\beta} \right) + d \tan 2\alpha \quad (4)$$

where $h_{B'}$ and $h_{A'}$ represent the distance between the points of incidence A' and B' and the screen of smartphone's plane P_G , l represents the distance between camera's plane P_C and outer circle B, d represents the distance between the two circles, α and β represent the tangent angles of cornea model at point A' and B' . The equation establishes that

the distance between any pair of circles-whether adjacent or not-is only determined by the difference in the distances between the points of incidence and the smartphone screen's plane, in conjunction with the tangent angles of the cornea model at these points of incidence. For those corneas with KC, both factors above - the difference in distances and the tangent angles - exhibit an increase.

The flowchart of our proposed diagnosis model and simultaneous experiment setup is illustrated in Figure 3c. In the first step of image collection, we designed and 3D-printed anatomically inspired eyeball models using the Bambu Lab X1 Carbon printer (Lab). These models incorporated variations in anterior chamber depth (ACD) to simulate different stages of keratoconus (normal, moderate, and severe). A custom L-shaped 3D-printed fixture was used to maintain a fixed 15 cm working distance and a consistent imaging angle between the corneal model and the light source. To minimize ambient reflections, the interior surfaces of the fixture were coated with black pigment. A Samsung Galaxy Note 20 Ultra (Samsung, 2020), with a peak screen brightness of 1500 nits, served as the light source and was positioned securely at the base of the setup. The smartphone cameras (iPhone XS MAX (Apple, 2023), iPhone 15 Pro (Apple, 2024a), iPhone 16 Pro (Apple, 2024b), and Galaxy Z Flip 3 (Samsung)) were used individually in the second step of image collection to capture raw Placido disc reflections from the corneal surface. Images were acquired under consistent exposure settings (3 seconds) and with auto-processing enabled. A total of 195 images were collected across devices and disease stages. In the third step, we applied reflection detection and image preprocessing algorithms to extract the Placido disc patterns from the side-view corneal reflections. These extracted features were then analyzed and classified into normal, moderate KC, and severe KC groups, and color-coded visualizations were generated to assist with diagnostic interpretation and visualization.

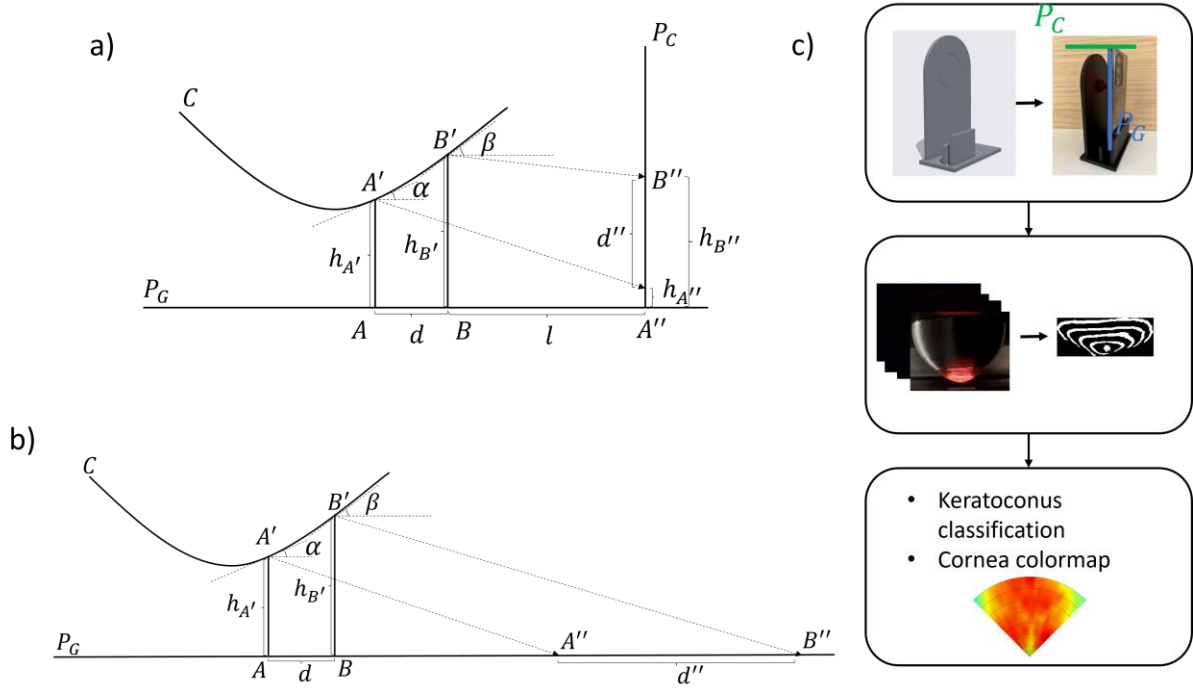


Figure 3. Principle and flowchart of 2-stage diagnosis. **a)** Schematic diagram of side-view image capturing using separate camera devices. **b)** Schematic diagram of traditional Placido disc-based diagnosis with coaxial camera-light source alignment. **c)** Flowchart of a simulation experiment for the 2-stage diagnosis.

2.2. Data preparation and preprocessing

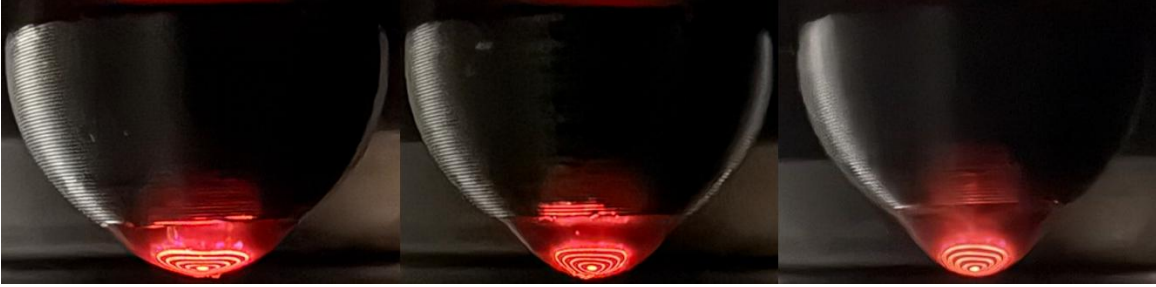
We used the Bambu Lab X1 Carbon 3D printer (Lab) to print the emulated eyeballs. This printer features a maximum build volume of $256 \times 256 \times 256 \text{ mm}^3$, allowing for the creation of models across our specified size range. We employed a 0.4 mm hardened steel nozzle and used Bambu PLA Basic filament with a diameter of $1.75 \text{ mm} \pm 0.03 \text{ mm}$, ensuring consistent extrusion and structural integrity. The enclosed building chamber, equipped with an activated carbon air filter, provided a stable printing environment, minimizing external influences on print quality. To emulate the reflective properties of the human cornea, we applied a reflective coating to the corneal region of each 3D-printed eyeball model (normal, moderate KC, and severe KC from top to bottom), as shown in Figure 4a. This approach effectively simulated the corneal reflection necessary for accurate analysis. In Figure 4b, we illustrate the L-shape instrument assisting image collection, which includes one round groove for fixing eyeball models and one holder for fixing the smartphone used as light source, and Figure 4c demonstrates the collected images from the eyeball models with different stage of KC.



(a)



(b)



(c)

Figure 4. 3D-printed eyeball models for experiment. **a)** Eyeball models over different severity of KC. **b)** L-shape model for fixing eyeball and light source. **c)** Original images from 3D-printed eyeball model (left to right: normal, moderate KC, severe KC)

We also designed a 5-circled Placido disc image that improves from the Placido discs of a keratoscope used in the optical clinic, as shown in Figure 1d-i. To validate the cross-device generalizability of our proposed method, we selected four commercially available smartphones with diverse hardware characteristics: Samsung Galaxy Z Flip 3, iPhone XS MAX, iPhone 15 Pro, and iPhone 16 Pro, as shown in Table 2. They have a fixed working distance of 15 cm to standardize reflection geometry. These devices represent a range of camera sensor configurations, lens types, and image optimization capabilities. The iPhone 15 Pro and iPhone 16 Pro are equipped with triple-lens systems

(including ultra-wide and telephotos), macro photography support, and advanced image processing for low-light conditions. Compared with them, the iPhone XS MAX and Galaxy Z Flip 3 have more limited camera arrays and lack macro functionality. All devices were used with the default camera application, fixed exposure settings (3 seconds), and auto-processing enabled to simulate practical deployment scenarios. Additionally, the Galaxy Note 20 Ultra—with a peak screen brightness of 1500 nits—was employed solely as the light source in the image acquisition setup.

Device	Galaxy Note 20 Ultra	iPhone 16 Pro	iPhone 15 Pro	Galaxy Z Flip 3	iPhone XS MAX
Role	Light source	Camera	Camera	Camera	Camera
Hardware Specifications and Features					
Screen					
Brightness (nits)	1500	-	-	-	-
Lens Type	-	Triple Camera	Triple Camera	Double Camera	Double Camera
Main	-	48MP, 24mm, f/1.78	48MP, 24mm, f/1.78	12MP, 27mm, f/1.8	12MP, 26mm, f/1.5
Wide	-	48MP, 24mm, f/1.78	48MP, 24mm, f/1.78	12MP, 27mm, f/1.8	12MP, 13mm, f/2.4
Ultra-Wide	-	48MP, 13mm, f/2.2	12MP, 13mm, f/2.2	12MP, 14mm, f/2.2	-
Telephoto	-	12MP, 120mm, f/2.8	12MP, 77mm, f/2.8	-	-
Camera Setting at Demonstrating System					
PDAF	-	Yes	Yes	Yes	Yes
Night Mode	-	Yes (3 Seconds Exposure)	Yes (3 Seconds Exposure)	Yes (3 Seconds Exposure)	Yes (3 Seconds Exposure)

Macro		Wide and	Yes		
photography	-	Ultra-Wide	Wide and	No	No
		Lens	Ultra-Wide Lens		
		Auto	Auto Processing		
Image		Processing for	for Low Light	Auto Processing	Auto
optimizing	-	Low Light	Density and	for Low Light	Processing for
algorithm		Density and	Macro	Density	Low Light
		Macro	Photography		Density
		Photography			

Table 2. The hardware specifications and image settings of smartphones used as light source and cameras in the proposed Keratoconus diagnostic system.

We applied specular reflection detection and removal to improve image quality by reducing the specular reflections in Placido disc images (Nie et al., 2023). In this study, we conducted imaging in a darkened room with an ambient illuminance of 7 lux, simulating the conditions commonly used in ophthalmic clinics. Initially, the system classifies the image based on brightness levels to identify regions with specular reflections. An adaptive threshold function, responsive to the image's brightness, is then applied to detect these reflective areas accurately. Once identified, the specular regions are restored using an exemplary-based inpainting algorithm, which reconstructs the occluded corneal features by referencing the surrounding texture information. This approach ensures that the Placido disc reflection patterns are accurately represented, enhancing the reliability of corneal curvature assessments.

For reflection extraction, we firstly applied a decision tree classification algorithm (Breiman, 2017) to extract the reflected Placido rings from the corneal images, due to the distinct color characteristics of the ring patterns (i.e., red hue relative to the background). Given the consistency and uniqueness of this color feature, we manually selected color-related features color-based features including HSV components, and normalized RGB values from the image pixels (Li et al.). These features capture hue, saturation, and chromaticity variations, effectively differentiating reflection patterns from surrounding non-informative regions. For example, we defined the input feature vector for each pixel as:

$$[pixel_H, pixel_S, pixel_V, \frac{R}{R+B+G}, \frac{G}{R+B+G}, chroma] \quad (5)$$

where $pixel_H$, $pixel_S$, and $pixel_V$ represent the pixel values in HSV color space (Sobottka & Pitas, 1996), R, G, B values are the pixel values at R, G, B channels of the images.

The decision tree algorithm operates by recursively partitioning the feature space based on threshold values learned during training. Each node in the tree represents a decision rule based on one feature, and the leaf nodes correspond to class labels indicating whether the pixel belongs to a reflected ring or background. Then, we retained the pixels that were predicted at the Placido graphic by the classification tree and generated a binary image.

Secondly, we applied an open-close operation (Soille, 1999) to denoise. Variance in the surface curvature of the cornea model can result in uneven light reflection (Urone & Hinrichs, 2016). Specifically, areas with more significant curvature tend to capture more light, appearing brighter in images (Healey & Kondepudy, 1994). Furthermore, the smartphone, which displays the 8-circle Placido disc, is the light source. As a result, areas closer to this light source also exhibit increased brightness.

Additionally, inherent noise in the camera sensor can contribute to disparities in the captured image. These factors collectively lead to color distortions in the original photos, which can interfere with binarization. To minimize the impact of color distortions, we applied an opening-closing operation (Soille, 1999). It is a morphological operation to reduce noise and enhance objects of interest. The opening operation is an erosion operation followed by dilation. It helps to remove small white objects not belonging to Placido circles in the binary image and smooth the boundary of the larger objects (Urone & Hinrichs, 2016). The closing operation is dilation followed by erosion. It helps to fill small holes and connect slightly disconnected objects.

Thirdly, we corrected the orientation (Lee et al., 2017) of the denoised image for further analysis. The processed binary image visualized the enhanced Placido rings, which included a central ellipse and a series of arcs. We located all the connected components in the image and found the central ellipse by identifying the element with white pixels in the central bottom area. The orientation, determined by the angle between the x-axis and the ellipse's central axis, was used to rotate the entire image and perform further analysis.

The final step is to focus on the region of interest by removing the irrelevant parts of the image. The bounding boxes (Lempitsky et al., 2009) of the ellipse and arcs define a rectangle for cropping.

A total of 232 images were collected across four smartphone models, encompassing three categories: normal, moderate keratoconus (KC), and severe KC. The dataset includes 42 images from the Galaxy Z Flip 3, 65 from the iPhone XS MAX, 58 from the iPhone 15 Pro, and 67 from the iPhone 16 Pro as shown in Table 3.

	Galaxy Z Flip 3	iPhone XS MAX	iPhone 15 Pro	iPhone 16 Pro
Normal	15	18	24	19
Moderate KC	16	22	22	19
Severe KC	16	25	12	29
Total	42	65	58	67

Table 3. Data distribution of collected corneal images across smartphone devices and different stages of Keratoconus (KC).

2.3. Weighted support vector machines

To classify corneal images into three categories: 1) normal, 2) moderate KC, and 3) severe KC, we employed a multiclass Weighted Support Vector Machine (WSVM) classifier (Yang et al., 2007). This approach efficiently handles class imbalances by assigning different weights to each class, thereby reducing the influence of underrepresented categories on the decision boundary. WSVM aims to find optimal hyperplanes that maximize the margin between classes while incorporating class-specific weights into its optimization problem. The optimization problem for WSVM is formulated in Eq. 6:

$$\text{Minimize } \phi(w) = \frac{1}{2}w^T w + C \sum W_i \xi_i \quad (6)$$

subject to:

$$y_i(\langle w, \phi(x_i) \rangle + b) \geq 1 - \xi_i, i = 1, \dots, l; \xi_i \geq 0, i = 1, \dots, l \quad (7)$$

where $x_i \in \mathbb{R}^d$ represents feature vector (i.e. width and height measurements from the Placido disc images), $y_i \in \{-1, 0, 1\}$ is the class labels correspond to normal, moderate KC, and severe KC respectively, w and b define the hyperplane, ξ_i are slack variables allowing for misclassification, C is the regularization parameter controlling the

trade-off between maximizing the margin and minimizing the classification error, and w_i are the weights assigned to each sample based on class distribution.

To extend the binary WSVM to multiclass classification, we applied the one-vs-one (OvO) strategy (Milgram et al., 2006), constructing a WSVM classifier for each pair of classes. A majority voting among all pairwise classifiers determine the final classification decision for a new sample. This method allows for fine-tuned decision boundaries sensitive to each class's characteristics.

However, they are sensitive to outliers, as these anomalous data points can significantly influence the position of the decision boundary, leading to reduced model performance. To reduce this effect, we applied Z-score normalization to the feature set to standardize the data, ensuring that each feature contributes equally to the distance calculations within the SVM algorithm. This preprocessing step enhances the model's performance by preventing larger-scale features from dominating the learning process and reducing the effect of outliers. The Z-score for a data point x is calculated in Eq. 8:

$$Z = \frac{x - \mu}{\sigma} \quad (7)$$

where μ represents the mean value, and σ is the standard deviation of the dataset. Data points with a Z-score exceeding a certain threshold (± 3) are considered outliers and can be excluded from the dataset. Removing these outliers makes the dataset allow the SVM to establish a more accurate decision boundary and reduces the influence of extreme values on the model's performance.

2.4. Analysis of Variance (ANOVA)

To evaluate whether there are statistically significant differences among the means of three independent groups—namely, normal, moderate keratoconus (KC), and severe KC—we employed a one-way Analysis of Variance (ANOVA) (Quirk & Quirk, 2012). This method is appropriate for comparing more than two group means and helps control the Type I error rate that would increase if multiple pairwise t-tests were conducted. ANOVA partitions the total variability in the data into variability between groups and within groups, allowing us to assess whether the between-group variability is significantly greater than what would be expected by chance. The test statistic for ANOVA is the F-ratio, calculated as:

$$F = \frac{MS_{between}}{MS_{within}} \quad (5)$$

where $MS_{between}$ is the mean square between groups, and MS_{within} is the mean square within groups. A significant F-ratio indicates that at least one group means differs from the others, warranting further post hoc analyses to identify specific group differences.

2.5. Omega Squared (ω^2)

While ANOVA determines the presence of statistically significant differences among group means, it does not convey the magnitude of these differences. To quantify the proportion of variance in the dependent variable attributable to group membership, we calculated omega squared (ω^2), an effect size measure. Omega squared is preferred over eta squared (η^2) because it provides a less biased estimate of the population effect size, particularly in studies with small sample sizes. The formula for omega squared in a one-way ANOVA is:

$$\omega^2 = \frac{SS_{between} - (df_{between} \times MS_{within})}{SS_{total} + MS_{within}} \quad (7)$$

where $SS_{between}$ is the sum of squares between groups, $df_{between}$ is the degrees of freedom between groups, MS_{within} is the mean square within groups, and SS_{total} is the total sum of squares. Omega squared values range from 0 to 1, with higher values indicating a greater proportion of variance explained by the group variable. This measure provides a more accurate reflection of the effect size in the population, enhancing the interpretability of our findings.

3. Results

3.1. Image preprocessing

In this paper, we applied a robust approach to extract reflected Placido discs as the diagram shown in Figure 5. We visually compare the original corneal image captured by the smartphone camera and the processed image after specular reflection detection and removal. In the original image (Figure 5a), obvious specular highlights are observed on the cornea model, which is caused by the reflection of the environment illumination source. These reflections can be detected in further image processing, potentially affecting the accuracy of analysis. After applying a brightness-based detection and exemplar-based inpainting method, the specular highlights were suppressed in the processed image (Figure 5b), and they

became smoother and gentler. This improvement enhances and contributes to more reliable feature extraction for keratoconus classification.

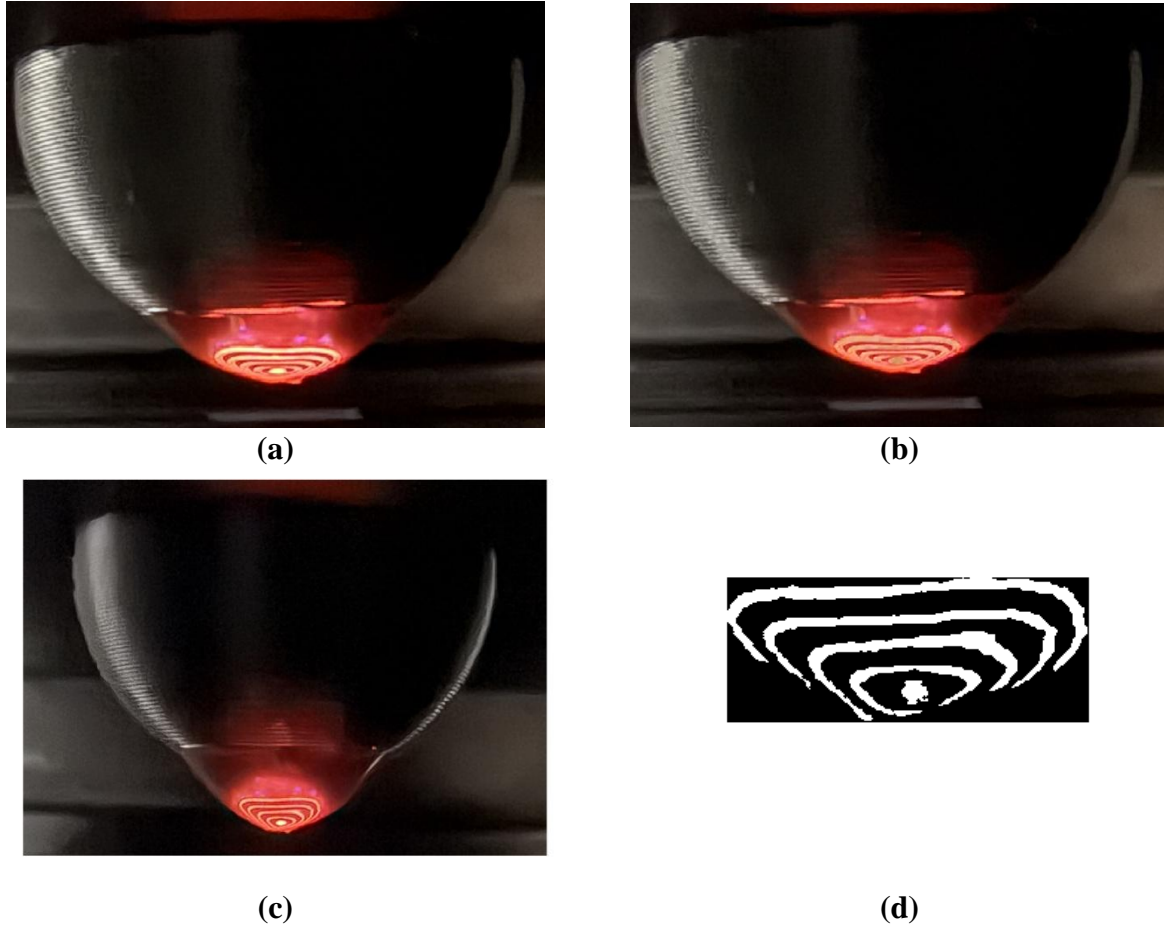


Figure 5. Preprocessing and extraction of Placido disc reflections for feature analysis. **a)** The original image from a normal group. **b)** The processed image after specular reflection detection and removal. **c)** The preprocessed image from severe KC group. **d)** The extracted reflection of Placido disc graphic.

3.2. Two-stage KC diagnosis – Classification

To evaluate the robustness and generalizability of our proposed method, we assessed performance across corneal images captured by different smartphone cameras: Samsung Galaxy Z Flip 3, iPhone XS MAX, iPhone 15 Pro, and iPhone 16 Pro, as shown in Figure 6 (a–d). Across all devices except iPhone XS MAX, the classifier achieved high specificity and sensitivity, particularly in identifying severe KC cases. This consistency suggests the model’s ability

to recognize morphological changes associated with severe KC, regardless of imaging source. Confusion was occasionally observed for moderate and normal classes, and different stages, especially in the iPhone XS MAX dataset (Figure 5b), where moderate KC was misclassified as severe and normal. This suggests that features at early stages may be more susceptible to variations in imaging conditions or reflective artifacts. Compared with the iPhone XS MAX, data from the iPhone 15 Pro and the iPhone 16 Pro had fewer misclassifications, demonstrating the model's capability to reduce intra-class variance and camera-dependent noise with more advanced camera specifications.

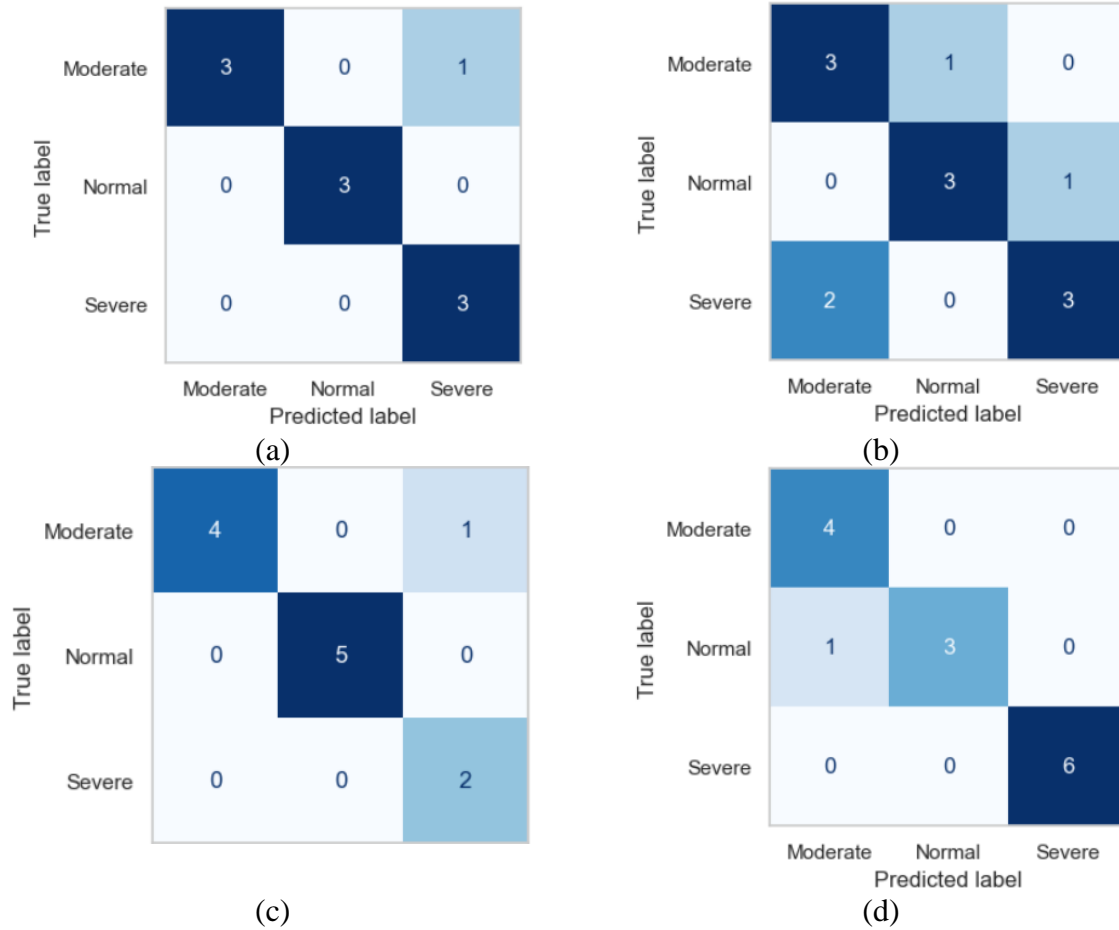


Figure 6. Confusion matrixes produced by weighted support vector machine (WSVM) for classifying corneal images captured by different smartphone cameras. a) Image data from Samsung Galaxy Z Flip 3. b) Image data from iPhone XS MAX. c) Image data from iPhone 15 Pro. d) Image data from iPhone 16 Pro.

Besides confusion matrices, we also evaluated the method with standard metrics (accuracy, precision, recall, and F1 score) with corresponding 95% confidence intervals, as shown in Table 3. All image data were acquired under controlled conditions with consistent lighting and fixed imaging angles to eliminate environmental variability. Among

the devices tested, the iPhone 16 Pro achieved the highest performance, with an accuracy of 92.93% (CI: 0.78–0.99), precision of 92.43%, recall of 91.24%, and an F1 score of 90.03%. Similarly, the iPhone 15 Pro showed strong and stable performance (accuracy: 91.57%, CI: 0.75–0.99), supporting the effectiveness of our system across advanced smartphone models.

The Samsung Galaxy Z Flip 3 was used solely in its unfolded form as a standard smartphone camera, demonstrating an accuracy of 90.04% (CI: 0.70–0.99) and an F1 score of 88.38%. These results establish a practical performance threshold, suggesting that any device achieving similar or higher metrics can be considered suitable for this diagnostic framework. In contrast, the iPhone XS MAX obtained an accuracy of only 68.95% (CI: 0.00–0.50) and correspondingly low scores in other metrics. Based on these findings, we designate the specifications of the Samsung Galaxy Z Flip 3 as the reference threshold, and consider devices performing below this baseline as unsuitable for clinical deployment within this system. In conclusion, the classification results demonstrate that the proposed system maintains high diagnostic accuracy, precision, and robustness across multiple smartphone models with varying hardware specifications..

	Performance metrics (95% CI)			
	Accuracy	Precision	Recall	F1
Samsung Galaxy Z Flip 3	90.04% (0.70-0.99)	90.45% (0.61-0.99)	90.57% (0.62-0.99)	88.38% (0.61-0.99)
iPhone XS MAX	68.95% (0.38-0.92)	69.16% (0.37-0.94)	69.26% (0.38-0.94)	66.14% (0.36-0.93)
iPhone 15 Pro	91.57% (0.75-0.99)	88.85% (0.67-0.99)	90.77% (0.58-0.99)	87.65% (0.60-0.99)
iPhone 16 Pro	92.93% (0.78-0.99)	92.43% (0.62-0.99)	91.24% (0.67-0.99)	90.03% (0.63-0.99)

Table 4. Average performance metrics (accuracy, precision, recall, and F1 score) over different smartphone cameras.

3.3. Two-stage KC diagnosis – Visualization

Keratoconus causes localized thinning and protrusion of the cornea altering its topography. KC does not appear at a fixed location but manifests anywhere on the cornea. Thus, we visualize a distance matrix to pinpoint the exact location of the protrusion. This distance map facilitates more accurate diagnosis and treatment planning, such as determining

suitable sites for corneal cross-linking or intracorneal ring segment (ICRS) placement, as performed conventionally in Alió's work (Alió et al., 2006).

We implemented a color scheme to enhance the interpretability of Keratoconus severity. This visual enhancement more effectively differentiates the levels of corneal protrusion, with individual colors indicating diverse depths. It allows us to visualize the exact location of KC on the cornea as shown in Figure 7.

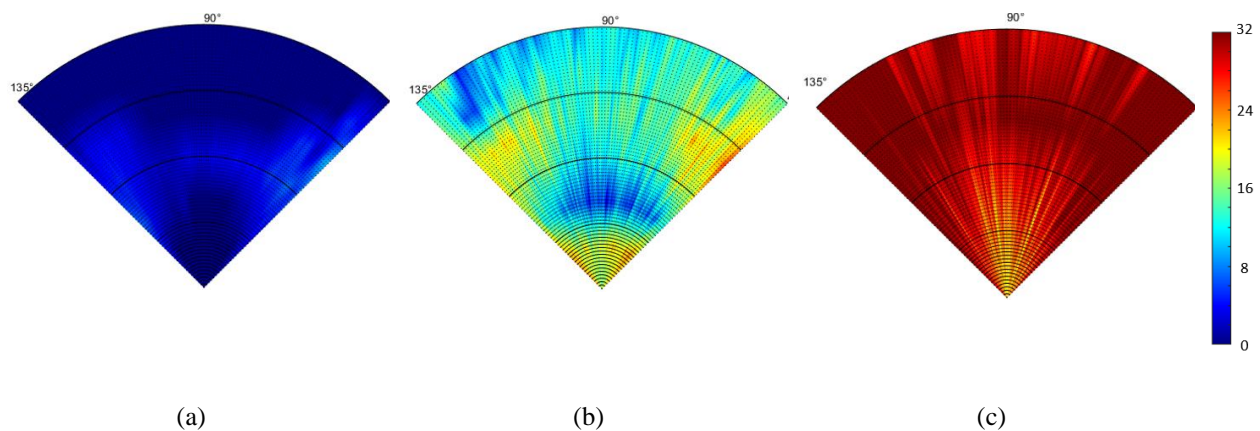
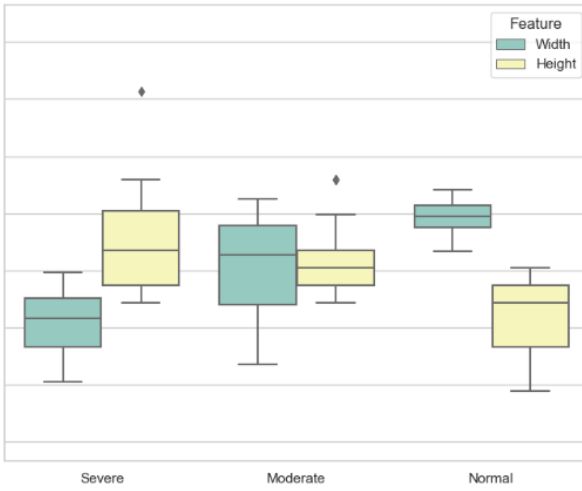


Figure 7. Color-coded distance maps visualizing Placido disc deformation across different stages of Keratoconus. **a)** Colormap of normal cornea. **b)** Colormap of moderate KC cornea. **c)** Colormap of severe KC cornea.

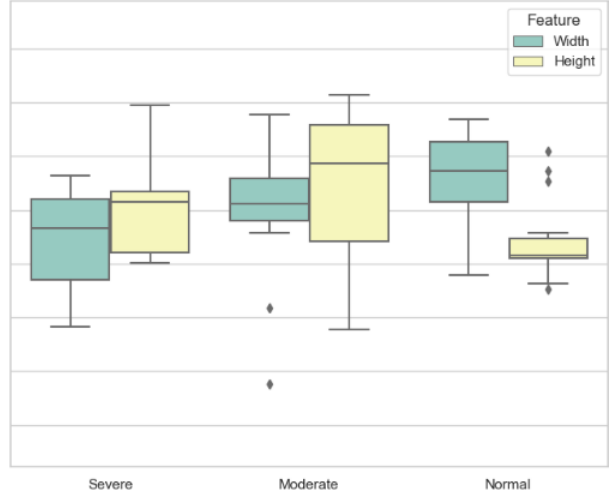
Spanning an angular range from 45 to 135 degrees, this visual improvement effectively distinguished varying inter-disc distances, with the color spectrum representing these distances. More blueish colors, such as blues and greens, were assigned to shorter distances, corresponding to healthier cornea states, while warmer hues, including oranges and reds, depicted longer distances caused by protrusion, indicating more severe KC conditions. As the colors transition from cool to warm, they suggest progression from normal status to severe KC-affected status, with the red tones indicating the most severe cases. The color map differentiates among normal and different stages of corneas and precisely visualizes the KC on the cornea, making it a valuable tool for accurate diagnosis and targeted treatment planning.

3.4. Statistical analysis

Figure 8 illustrates the standardized width and height feature distribution of each device across keratoconus severity levels. In all cases, height decreases by increasing disease severity, supporting its value as a consistent geometric marker of disease and its severity. The separation between classes is most distinct in the iPhone 16 Pro (Figure 8d), where the interquartile ranges are well-separated with minimal overlap. Conversely, the iPhone XS MAX (Figure 8b) exhibits more significant variability and class overlap, particularly in the height feature, which contributes to its lower classification performance.



(a)



(b)

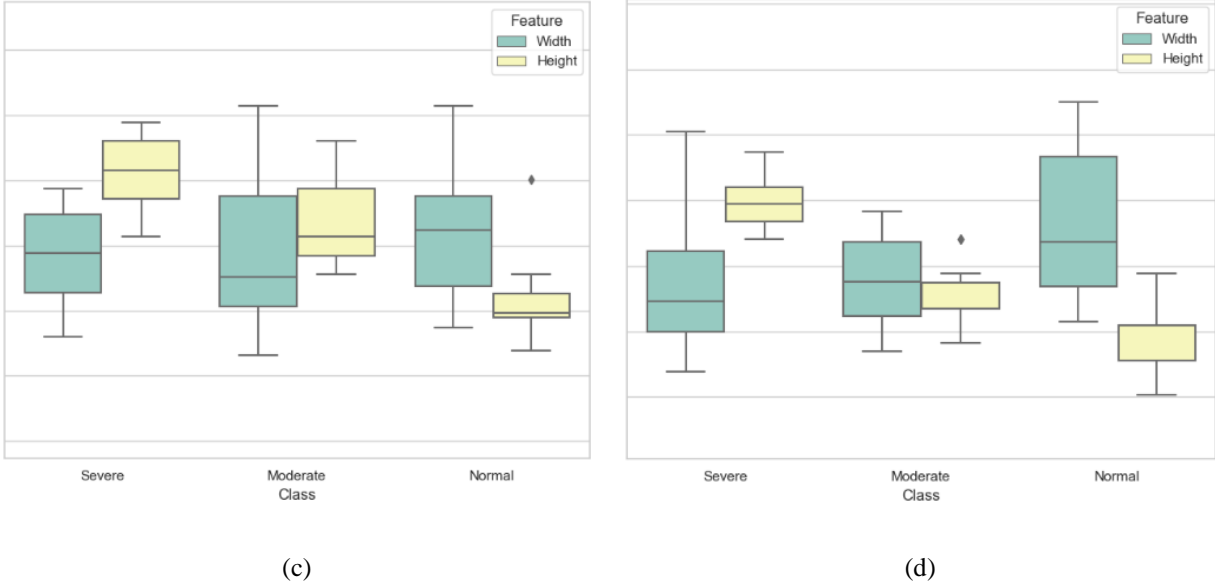


Figure 8. oxplots of standardized width and height features extracted from corneal reflection images captured by different smartphone cameras. a) Boxplot from Galaxy Z Flip 3. b) Boxplot from iPhone XS MAX. c) Boxplot from iPhone 15 Pro. d) Boxplot from iPhone 16 Pro.

Table 5 summarizes the results of one-way ANOVA and corresponding Omega Squared (ω^2) effect sizes for standardized width and height measurements across keratoconus severity levels on different smartphone devices. Across all devices, height consistently demonstrated stronger discriminatory power than width, with the highest effect sizes observed on iPhone XS MAX and iPhone 16 Pro ($\omega^2 = 0.8398$), indicating that height captures substantial variance associated with disease stage. The Samsung Galaxy Z Flip 3 also showed large effect sizes for width ($\omega^2 = 0.5435$) and height ($\omega^2 = 0.3302$), confirming its suitability as a performance threshold. In contrast, width measurements from iPhone 15 Pro showed no significant group differences ($\omega^2 = -0.0212$), suggesting that device-specific optical factors may influence the reliability of certain features.

Device	Feature	F-value	p-value	ω^2
Samsung Z Flip 3	Width	28.98	9.33×10^{-9}	0.5435
	Height	12.58	4.80×10^{-5}	0.3302
iPhone XS MAX	Width	8.61	0.0005	0.1897

iPhone 15 Pro	Height	7.93	0.0009	0.1758
	Width	0.40	0.6740	-0.0212
iPhone 16 Pro	Height	55.78	5.85×10^{-14}	0.6538
	Width	4.59	0.0138	0.0967
	Height	176.60	8.85×10^{-27}	0.8398

Table 5. One-way ANOVA and corresponding Omega Squared (ω^2) effect sizes for standardized width and height measurements across keratoconus severity levels on different smartphone devices.

4. Conclusion

Placido disc technology and its computer analysis have long been an established method for diagnosing keratoconus. However, it requires operator experience and is costly. This manuscript introduces a novel application of Placido disc technology using a smartphone platform. We utilize the smartphone camera to capture distinctive corneal images, enabling a novel data extraction and analysis approach.

In our approach, we modified the traditional Placido disc by replacing the empty central ring with a solid circle, significantly improving the accuracy and consistency of the extracted reflection. As shown in Figure 3, compared to the empty ring design, the solid circle allows for the entire reflected shape to form a well-defined ellipse. This complete reflection enables precise orientation correction by detecting the long axis of the reflected shape and rotating it accordingly. With a consistently aligned reflection, subsequent feature extraction becomes more reliable. Specifically, for distance matrix generation, the rays used to compute inter-disc distances will always originate from a fixed starting point, which is the center of the solid reflected ellipse, minimizing the bias in distance measurements compared to the fragmented reflections from a traditional Placido disc that is hard to localize the center. Furthermore, when measuring the height and width of the extracted Placido disc reflection, the corrected orientation ensures more accurate dimension estimation, reducing errors caused by misalignment. This refinement ultimately enhances the overall precision of keratoconus classification and visualization.

In summary, our proposed WSVM-based classification framework demonstrates robust and accurate performance across various smartphone cameras, suggesting its potential as a reliable tool for keratoconus severity classification. Our

proposed method achieved high accuracy, precision, recall, and F1 scores with advanced devices such as the iPhone 15 Pro, iPhone 16 Pro, and Samsung Galaxy Z Flip 3. Particularly, the classifier can reliably detect severe KC cases across all tested devices, indicating its sensitivity to the morphological changes associated with advanced disease stages.

By setting the Samsung Galaxy Z Flip 3 as a practical baseline threshold, we propose a baseline to evaluate smartphone suitability in clinical diagnostic contexts. Devices that exceed this performance threshold, such as the iPhone 15 Pro and iPhone 16 Pro, were shown to be well-suited for accurate KC classification. On the other hand, even if the imaging conditions are controlled, the significantly degraded performance observed with the iPhone XS MAX demonstrates that hardware or software limitations can reduce the system's reliability. These findings underscore the significance of camera quality and reinforce the system's suitability for deployment in portable, cost-effective settings, as device specifications meet the required standards.

Previous studies that rely on conventional Placido disc-based topographers, such as the work by Kamiya et al. (Kamiya et al., 2021), which used TMS-4TM equipment and deep learning on color-coded topography maps to achieve high classification accuracy (96.6%) and sensitivity (98.8%) for keratoconus detection, and 78.5% accuracy in classifying the stage. While traditional systems require costly, stationary clinical instrumentation and specialized acquisition software, our smartphone-based system captures raw reflection patterns directly from the cornea using readily available consumer devices under controlled but portable conditions. Despite using simplified imaging inputs without full surface curvature reconstruction, our approach achieves comparable classification performance, with the added advantage of enabling point-of-care deployment and broader accessibility in low-resource or non-clinical settings.

Based on the comparative evaluation, we suggest using the hardware and imaging performance of the Samsung Galaxy Z Fold 3 as a minimum threshold for clinical applicability to ensure reliable diagnostic outcomes. This device features a dual-camera system with a 12MP main lens (27 mm, f/1.8) and a 12MP ultra-wide lens (14 mm, f/2.2), along with night mode support (3-second exposure) and automatic processing for low-light environments. The classifier achieved over 90% accuracy and an F1 score of 88.38%, with images captured using this setup under consistent acquisition protocols. Devices lacking key capabilities such as macro photography support or advanced computational enhancement, like the iPhone XS MAX, exhibited substantially poorer performance (accuracy: 16.48%, F1 score: 11.60%) under the same imaging conditions.

In addition to classification performance, statistical analyses were conducted to validate the reliability and discriminative strength of the extracted features. One-way ANOVA and Omega Squared (ω^2) confirmed that the height feature exhibited large effect sizes across most devices, particularly for the iPhone 16 Pro ($\omega^2 = 0.8398$), indicating a strong association with KC severity. Furthermore, classification metrics were evaluated using a 1,000-iteration bootstrapping approach, yielding narrow 95% confidence intervals for high-performing devices, such as the iPhone 15 Pro and iPhone 16 Pro. These results affirm the robustness of the proposed features and support the statistical reliability of the system's diagnostic performance across various device configurations.

Our comprehensive analysis helped distinguish normal corneas from those suffering from Keratoconus, recognize different stages of the cornea, and provide the location of the KC. A noteworthy addition was the inclusion of a color map in the distance matrix, which improved the precise visualization of KC on the cornea and enhanced diagnostic accuracy. This innovative technique can refine treatment strategies by providing a clear visualization of the affected areas. Due to widespread use of smartphones, our approach facilitates access to advanced diagnostic tools, making them available to a broader audience, including those in remote or underserved areas. It enables rapid and convenient preliminary screening for keratoconus, eliminating the need for specialized equipment or trained personnel. In future work, we plan to conduct comprehensive clinical trials to assess the efficacy and accuracy of our diagnostic method. This will include gathering data from patients with different severities of keratoconus and exploring the integration of additional diagnostic modalities, such as corneal biomechanics and tomography, to ensure the model's robustness and reliability in real-world applications.

5. REFERENCES

- Alió, J. L., Shabayek, M. H., & Artola, A. (2006). Intracorneal ring segments for keratoconus correction: long-term follow-up. *Journal of Cataract & Refractive Surgery*, 32(6), 978-985.
- Apple. (2023). *iPhone 14*. <https://www.apple.com/go/2023/iphone-14/>
- Apple. (2024a). *iPhone 15 Pro - Tech Specs*. <https://support.apple.com/en-us/111829>
- Apple. (2024b). *iPhone 16 Pro*. <https://www.apple.com/iphone-16-pro/specs/>
- Askarian, B., Tabei, F., Askarian, A., & Chong, J. W. (2018). An affordable and easy-to-use diagnostic method for keratoconus detection using a smartphone. *Medical imaging 2018: computer-aided diagnosis*,
- Breiman, L. (2017). *Classification and regression trees*. Routledge.
- Cavas-Martínez, F., De la Cruz Sánchez, E., Nieto Martínez, J., Fernández Cañavate, F., & Fernández-Pacheco, D. Corneal topography in keratoconus: State of the art. *Eye Vis (Lond)*. 2016; 3: 5. In.
- Emre, S., Doganay, S., & Yologlu, S. (2007). Evaluation of anterior segment parameters in keratoconic eyes measured with the Pentacam system. *Journal of Cataract & Refractive Surgery*, 33(10), 1708-1712.

- Farjo, A. A., McDermott, M. L., & Soong, H. K. (2009). Corneal anatomy, physiology, and wound healing. *Ophthalmology*, 44(2), 203-208.
- Fu, P.-I., Fang, P.-C., Ho, R.-W., Chao, T.-L., Cho, W.-H., Lai, H.-Y., Hsiao, Y.-T., & Kuo, M.-T. (2020). Determination of tear lipid film thickness based on a reflected placido disk tear film analyzer. *Diagnostics*, 10(6), 353.
- Gao, M., Wu, C., Li, B., Sheng, B., & Huang, Y. (2020). Design and implementation of a Placido disk-based corneal topographer optical system based on aberration theory and simulated annealing algorithm. *Optics Communications*, 475, 126097.
- Hashemi, H., Yekta, A., Yazdani, N., Ostadimoghaddam, H., & Khabazkhoob, M. (2020). Comparison of anterior chamber depth between normal and keratoconic eyes: a systematic review and meta-analysis. *Journal of Current Ophthalmology*, 32(1), 94-98.
- Kamiya, K., Ayatsuka, Y., Kato, Y., Shoji, N., Mori, Y., & Miyata, K. (2021). Diagnosability of keratoconus using deep learning with Placido disk-based corneal topography. *Frontiers in Medicine*, 8, 724902.
- Kovács, I., Németh, J., & Nagy, Z. Z. (2010). Anterior chamber characteristics of keratoconus assessed by rotating Scheimpflug imaging. *Journal of Cataract & Refractive Surgery*, 36(7), 1101-1106.
- Lab, B. *Bambu Lab X1C 3D Printer*. <https://us.store.bambulab.com/products/x1-carbon?srsltid=AfmBOooBCBnMn5i5D6H1PFN6cRAslWAXkdMsEdLqPKagQbsvaAxDYvbf>
- Li, Y., Pang, A. W., & Chong, J. W. A Robust Approach to Segment Human Skin and Burnt Region from Chaos Background Using Classification Trees.
- Mejía-Barbosa, Y., & Malacara-Hernández, D. (2001). A review of methods for measuring corneal topography. *Optometry and vision science*, 78(4), 240-253.
- Milgram, J., Cheriet, M., & Sabourin, R. (2006). “One against one” or “one against all”: Which one is better for handwriting recognition with SVMs? tenth international workshop on Frontiers in handwriting recognition,
- Næser, K., Savini, G., & Bregnhøj, J. F. (2016). Corneal powers measured with a rotating Scheimpflug camera. *British Journal of Ophthalmology*, 100(9), 1196-1200.
- Nie, C., Xu, C., Li, Z., Chu, L., & Hu, Y. (2023). Specular reflections detection and removal for endoscopic images based on brightness classification. *Sensors*, 23(2), 974.
- Quirk, T. J., & Quirk, T. J. (2012). One-way analysis of variance (ANOVA). *Excel 2007 for educational and psychological statistics: A guide to solving practical problems*, 163-179.
- Samsung. *Galaxy Z Flip 3*. <https://www.samsung.com/levant/smartphones/galaxy-z-flip3-5g/specs/>
- Samsung. (2020). *Galaxy Note20 5G / Note20 Ultra 5G*. <https://www.samsung.com/us/smartphones/galaxy-canvas/>
- Seitz, B., Behrens, A., & Langenbucher, A. (1997). Corneal topography. *Current opinion in ophthalmology*, 8(4), 8-24.
- Shirayama, M., Wang, L., Koch, D. D., & Weikert, M. P. (2010). Comparison of accuracy of intraocular lens calculations using automated keratometry, a Placido-based corneal topographer, and a combined Placido-based and dual Scheimpflug corneal topographer. *Cornea*, 29(10), 1136-1138.
- Wang, M. (2024). *Corneal Topography: A Guide for Clinical Application in Wavefront Era*. CRC Press.
- Yang, X., Song, Q., & Wang, Y. (2007). A weighted support vector machine for data classification. *International Journal of Pattern Recognition and Artificial Intelligence*, 21(05), 961-976.